

Aqueous MXene/Xanthan Gum Hybrid Inks for Screen-Printing Electromagnetic Shielding, Joule Heater, and Piezoresistive Sensor

Han Wu, Yimei Xie, Yanan Ma, Binbin Zhang, Bin Xia, Pengxiang Zhang, Wei Qian, Daping He, Xin Zhang, Bao-Wen Li,* and Ce-Wen Nan

MXenes have exhibited potential for application in flexible devices owing to their remarkable electronic, optical, and mechanical properties. Printing strategies have emerged as a facile route for additive manufacturing of MXene-based devices, which relies on the rational design of functional inks with appropriate rheological properties. Herein, aqueous MXene/xanthan gum hybrid inks with tunable viscosity, excellent printability, and long-term stability are designed. Screen-printed flexible MXene films using such hybrid inks exhibit a high conductivity up to $4.8 \times 10^4 \text{ S m}^{-1}$, which is suitable to construct multifunctional devices mainly including electromagnetic shielding, Joule heaters, and piezoresistive sensors. The average electromagnetic interference (EMI) shielding value can reach to 40.1 dB. In the Joule heater, the heating rate of printed MXene film can reach $20 \text{ }^\circ\text{C s}^{-1}$ under a driving voltage of 4 V, with a highest steady-state temperature of $130.8 \text{ }^\circ\text{C}$. An MXene-based piezoresistive sensor prepared by the printing interdigital electrode also presents good sensing performance with a short response time of 130 ms and wide pressure region up to 30 kPa. As a result, screen-printed MXene film exhibits reinforced multifunctional performance, which is promising for application in the next-generation of intelligent and wearable devices.

flexible devices with different sizes.^[1–3] Although several patterning methods, such as lithography, spray-masking and laser cutting, have been used for facile fabrication of those devices, the complicated processing and excessive material consumption in these protocols limit the scalable production of flexible devices.^[4] So far, it remains a significant challenge to achieve multifunctional devices such as EMI shielding,^[5] Joule heater,^[6] sensor,^[7–9] radio frequency identification (RFID) tags,^[10] and energy storage unit^[11] by using simple and low-cost methods. In addition, seeking a suitable material is vital to develop and design high-performance multifunctional devices in low cost.

Recent progress in liquid-phase exfoliation of two-dimensional (2D) nanomaterials has highlighted the rational design of functional inks for additive manufacturing of high-performance devices with complex architectures based on printing strategies, such as screen printing, gravure printing and inkjet printing.^[12] Screen printing among them is of critical importance to manufacture integrated multifunctional devices by formulating functional inks, without using expensive and complicate equipment.^[13] Specially, screen printing provides the highest deposition rate (per unit time deposition material weight) than other printing technologies.^[14] One of the main challenges lies in formulation of functional inks with appropriate rheological properties, which are prerequisite for screen-printing multifunctional devices with high resolution.^[15,16]

As a new family of 2D layered transition metal carbides or nitrides, MXenes have become promising candidate for formulation of printable inks because of their remarkable electronic, optical, and mechanical properties.^[17] Generally, MXenes are usually synthesized by selectively etching A layer in the precursor of MAX phase. They can be represented by $\text{M}_{n+1}\text{X}_n\text{T}_x$, where M is the early transition metal, X stands for carbon and/or nitrogen, and T_x represents the terminal hydroxyl, oxygen, or fluorine groups.^[18,19] As a result, MXenes offer solution processing capabilities owing to their superior hydrophilicity and high negative surface charge.^[20] Clay-like behavior of MXene slurry and the formation of stable colloidal suspension have thus facilitated the fabrication of conducting films, nanocomposites, coatings and fibers for applications in energy


1. Introduction

The emergence of intelligent and wearable electronic systems has greatly accelerated the development of next generation of

H. Wu, Y. Xie, Y. Ma, B. Zhang, P. Zhang, X. Zhang, B.-W. Li
State Key Laboratory of Advanced Technology for Materials Synthesis and Processing
Center of Smart Materials and Devices
Wuhan University of Technology
Wuhan 430070, P. R. China
E-mail: bwli@whut.edu.cn

B. Xia, W. Qian, D. He
Hubei Engineering Research Center of RF-Microwave Technology and Application
Wuhan University of Technology
Wuhan 430070, P. R. China

C.-W. Nan
State Key Lab of New Ceramics and Fine Processing
School of Materials Science and Engineering
Tsinghua University
Beijing 100084, P. R. China

 The ORCID identification number(s) for the author(s) of this article can be found under <https://doi.org/10.1002/sml.202107087>.

DOI: 10.1002/sml.202107087

storage, electromagnetic shielding, and sensors.^[21,22] Considerable efforts so far have focused on the formulation of various MXene inks by including the additives like carbon nanotubes (CNTs), graphene, layered double hydroxides, cellulose and so on.^[23–25] The additives of cellulose and polymers were proposed to improve the dispersion and stabilization of MXene inks, while CNTs and graphene to create interconnected networks in the printed MXene films. Although these MXene inks exhibited excellent printability, the electrical conductivity of the printed MXene films was moderate ($<1 \times 10^4 \text{ S m}^{-1}$). In addition, the addition of inorganic additives will result in complicated processability and high cost of MXene inks. The high loading of dissimilar inorganic components may hinder highly dense structure formed in the printed MXene films. Ideally, low content of additives or even additive-free in MXene inks would be promising for scalable production of MXene-based devices.^[3,26]

In this work, aqueous MXene inks have been formulated by tuning the weight ratio between exfoliated MXene and xanthan gum. Such hybrid inks were environment friendly, and offered tunable viscosity, excellent printability and long-term stability. The hybrid inks can be screen-printed into diverse patterns with high conductivity and excellent mechanical flexibility, all contributing to the fabrication of multifunctional devices with outstanding EMI, Joule heater and piezoresistive sensor performances. The average EMI SE value of a 12 μm -thick MXene film printed on paper reaches 40.1 dB, with a maximum shielding efficiency of 98.55% maintained after bending

1000 cycles. A maximum steady-state temperature of the printed MXene film can reach 130.8 $^\circ\text{C}$, with a high heating rate up to 20 $^\circ\text{C s}^{-1}$ under the driving voltage of 4 V. The piezoresistive sensor deposited on paper has relatively short response time and recovery time ($<130 \text{ ms}$), and can detect pressure up to 30 kPa.

2. Results and Discussion

2.1. Synthesis of MXene

Al layer in the Ti_3AlC_2 powder can be removed by selectively etching in the mixed solution of hydrochloric acid (HCl) and lithium fluoride (LiF). **Figure 1a** depicts the X-ray diffraction (XRD) patterns of MAX phase before and after etching in HCl/LiF mixture. All diffraction peaks observed in MAX phase can be well indexed by standard card number (PDF card number: 52-0875). MAX phase belongs to $P6_3/mmc$ space group and its crystal structure is hexagonal symmetry. After etching, the obvious downshifts of the 002 peak can be attributed to the intercalation of hydroxyl, fluorine ions and water molecules.^[23] Meanwhile, the disappeared 104 peak indicated the fracture of Ti–Al bond as a consequence of complete etching.^[27] As shown in **Figure 1b,c**, the tightly stacked Ti_3AlC_2 MAX powder was transformed into accordion-like multilayer $\text{Ti}_3\text{C}_2\text{T}_x$ after etching, and further delaminated into $\text{Ti}_3\text{C}_2\text{T}_x$ nanosheets

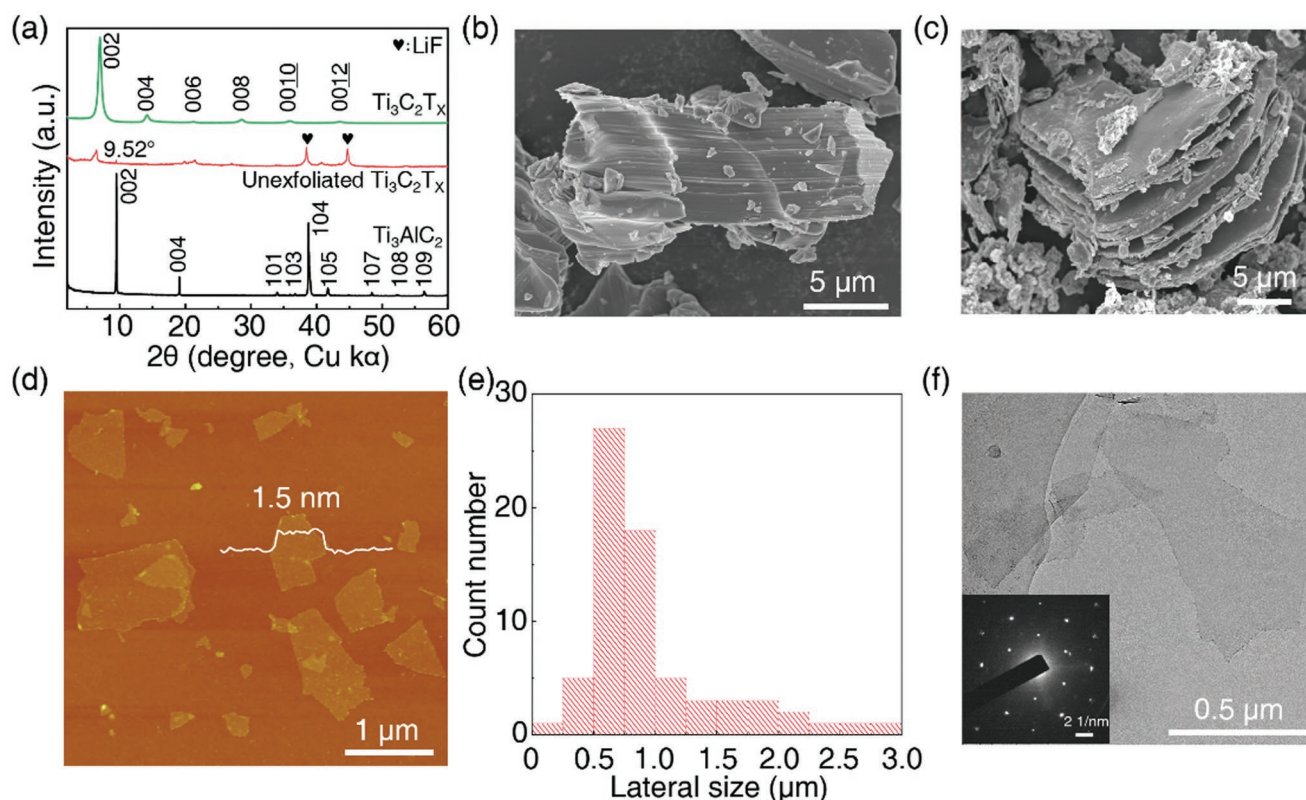


Figure 1. a) XRD patterns of Ti_3AlC_2 MAX, etched precursor and $\text{Ti}_3\text{C}_2\text{T}_x$ film fabricated by vacuum filtration. Scanning electron microscopy (SEM) images of b) Ti_3AlC_2 and c) as-etched $\text{Ti}_3\text{C}_2\text{T}_x$ powders. d) AFM image of $\text{Ti}_3\text{C}_2\text{T}_x$ MXene. e) Lateral size distribution of $\text{Ti}_3\text{C}_2\text{T}_x$. f) TEM image of exfoliated $\text{Ti}_3\text{C}_2\text{T}_x$. Inset shows the corresponding SAED pattern.

under ultrasonic treatment. Obvious Tyndall effect observed in the $Ti_3C_2T_x$ aqueous suspension suggests well dispersion of MXene in water (Figure S1, Supporting Information). Atomic force microscopy (AFM) image revealed that the thickness of exfoliated MXene was about 1.5 nm, while the size mainly distributed between 0.5 and 1.0 μm (Figure 1d,e). Transmission electron microscopy (TEM) image also revealed the transparent, flexible features for exfoliated MXene (Figure 1f). A typical hexagonal symmetric structure was confirmed by selected area electron diffraction (SAED) in the inset of Figure 1f, indicating the remained carbide crystal structure after exfoliation.^[28] The corresponding energy dispersive spectrometer implied that Ti, C, F, and O elements were uniformly distributed on the exfoliated MXene (Figure S2, Supporting Information).

X-ray photoelectron spectroscopy (XPS) was employed to analyze the chemical state of MXene (Figure S3, Supporting Information). In the Ti 2p spectra, a pair of asymmetric peaks appearing at 455.4 and 461.6 eV corresponded to Ti–C bond, while two sets of peaks at 455.8 and 461.8 eV were attributed to Ti^{2+} suboxide and/or hydroxide, at 456.9 and 463.1 eV to Ti^{3+} suboxide and hydroxide, and at 459.2 and 464.2 eV to TiO_2 phase (Figure S3b, Supporting Information). Moreover, substantial contribution from the Ti–O bond suggests that barely oxidation level occurred in the resultant MXene.^[29] A sharp peak located at 282.1 eV in C 1s spectrum indicates the existence of C–Ti bond in $Ti_3C_2T_x$ (Figure S3c, Supporting Information). In O 1s spectrum, the binding energies located at 529.9, 531.2, and 532.0 eV were attributed to the Ti–O, O^{2-} and OH^- terminations,

respectively (Figure S3d, Supporting Information).^[30] Functional groups including oxygen, fluorine, and chlorine terminations decorated on MXene endow it good hydrophilicity, which is conducive to ink formulation of MXene.^[31]

2.2. Ink Formulation of MXene and Screen-Printed MXene Film

The formulation process of MXene/xanthan gum hybrid inks is shown in Figure 2a. The ratios of MXene to xanthan gum were set as 150:6, 200:4, and 280:2, yielding three hybrid inks termed as hybrid ink-1, hybrid ink-2 and hybrid ink-3, respectively. Such hybrid inks obtained exhibited shear thinning behavior of non-Newtonian fluid in Figure 2b, regardless of MXene concentrations. As expected, xanthan gum plays an important role in adjusting the viscosity and modulus of MXene hybrid inks. The viscosity decreased with the increase of shear rate, which is necessary for continuous flow of printable inks. At the initial shear rate of $10^{-2} s^{-1}$, hybrid ink-3 has high viscosity above $10^4 Pa s$, which enable print out of high-resolution patterns in order to prevent short circuit. When the hybrid inks were inverted, they can still tightly adhere to the bottle wall, implying its viscous nature. Figure 2c displays the storage modulus (G') and loss modulus (G'') of hybrid ink-3 and pure MXene inks. Under low shear stress below 100 Pa, G' value was an order of magnitude higher than G'' , indicative of its elastic behavior.^[32] Hybrid ink-3 can withstand larger yield stress up to 146.25 Pa which is much higher than 68.9 Pa for pure MXene inks. When the shear

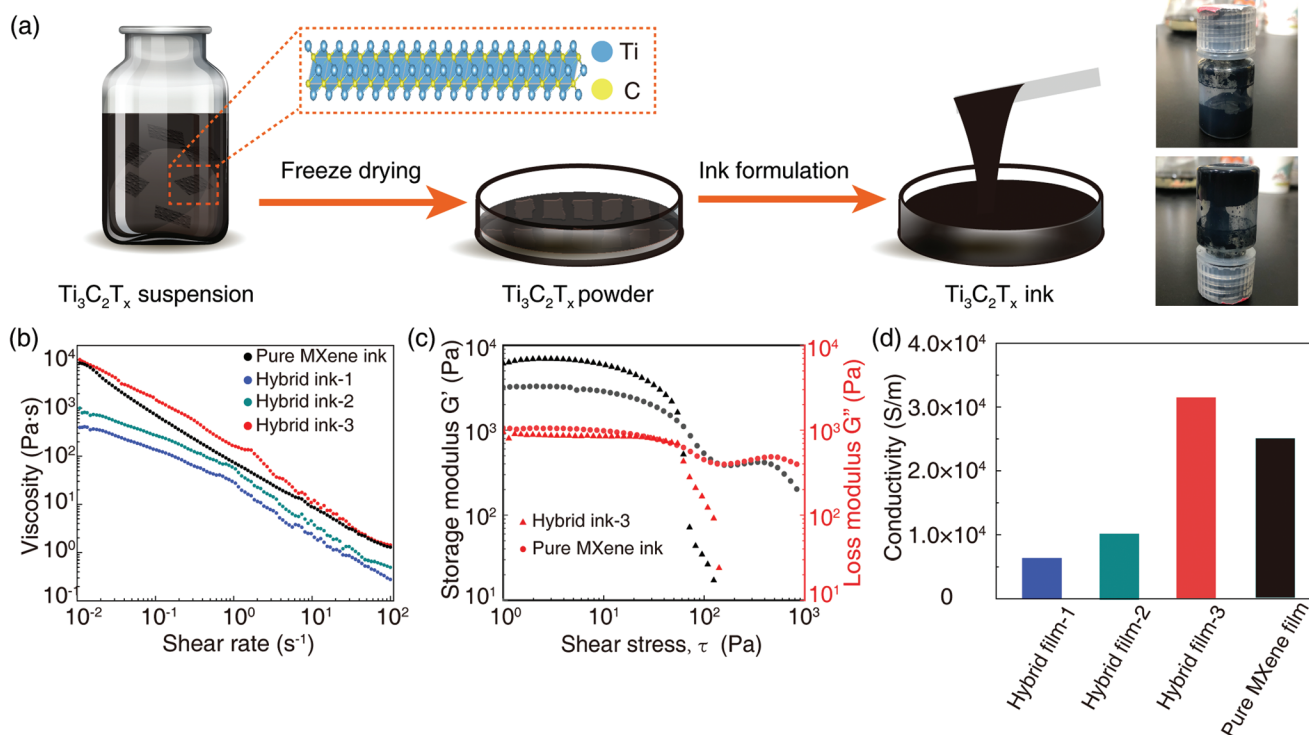


Figure 2. a) Schematic illustration of MXene ink formulation. Right part is the optical photographs of hybrid ink-3 in the normal and inverted states. b) Viscosity shear stress curves of MXene/xanthan gum hybrid inks with different concentrations. The concentration of pure MXene ink is 280 mg mL⁻¹. c) Storage modulus and loss modulus of hybrid ink-3 and pure MXene inks plotted as a function of shear stress. d) Conductivity of screen-printed MXene films with different weight ratios of MXene to xanthan.

stress was increased above 300 Pa, G'' played a dominating role, which is favorable for MXene hybrid inks to be extruded from the mesh onto the target substrate. The conductivity of printed MXene patterns was found to increase with the increase of MXene/xanthan weight ratio (Figure 2d), with a maximum conductivity at 280 mg mL⁻¹. As compared to pure MXene films, the relatively high conductivity of printed MXene film using hybrid inks is associated with the dense stacking of MXene nanosheets (Figure S4, Supporting Information). The concentration of MXene hybrid inks was thus fixed as 280 mg mL⁻¹ to construct diverse flexible devices using screen printing method in Figure 3a. To improve the adhesion between MXene hybrid inks and flexible substrates, polyethylene terephthalate (PET) and polyimide (PI) films were treated by UV for 1h to improve their wettability. As shown in Figure S4 (Supporting Information), the contact angles for water droplets on PET and PI films decreased from 91.3° to 30.4°, 79.9° to 40.3°, respectively, while

51.2° on photographic paper (Figure S5a, Supporting Information). Along with the decrease of contact angles, the improved wettability is conducive to high-resolution screen-printing.^[33] Figure 3b₁,b₂ shows optical photographs of a series of MXene patterns with complicated shapes printed on paper and PET substrates. Meanwhile, Figure 3b₃ shows the local amplification region in Figure 3b₂, with lines in parallel to each other (line width: ≈800 μm; line spacing: ≈400 μm). The printed line widths can be tuned from 400 to 2000 μm, suggesting good printing accuracy (Figure S6, Supporting Information).

MXene hybrid inks are printable regardless of the choice of substrate. Figure 3c₁ illustrates optical photographs of the integrity of MXene film printed on PET substrate, similar integrity was also observed on the MXene patterns printed on paper and PI substrates (Figure S7a₁,b₁, Supporting Information). As shown in Figure 3c₂ and Figure S7a₂,b₂ (Supporting Information), highly dense and uniform MXene films were achieved.

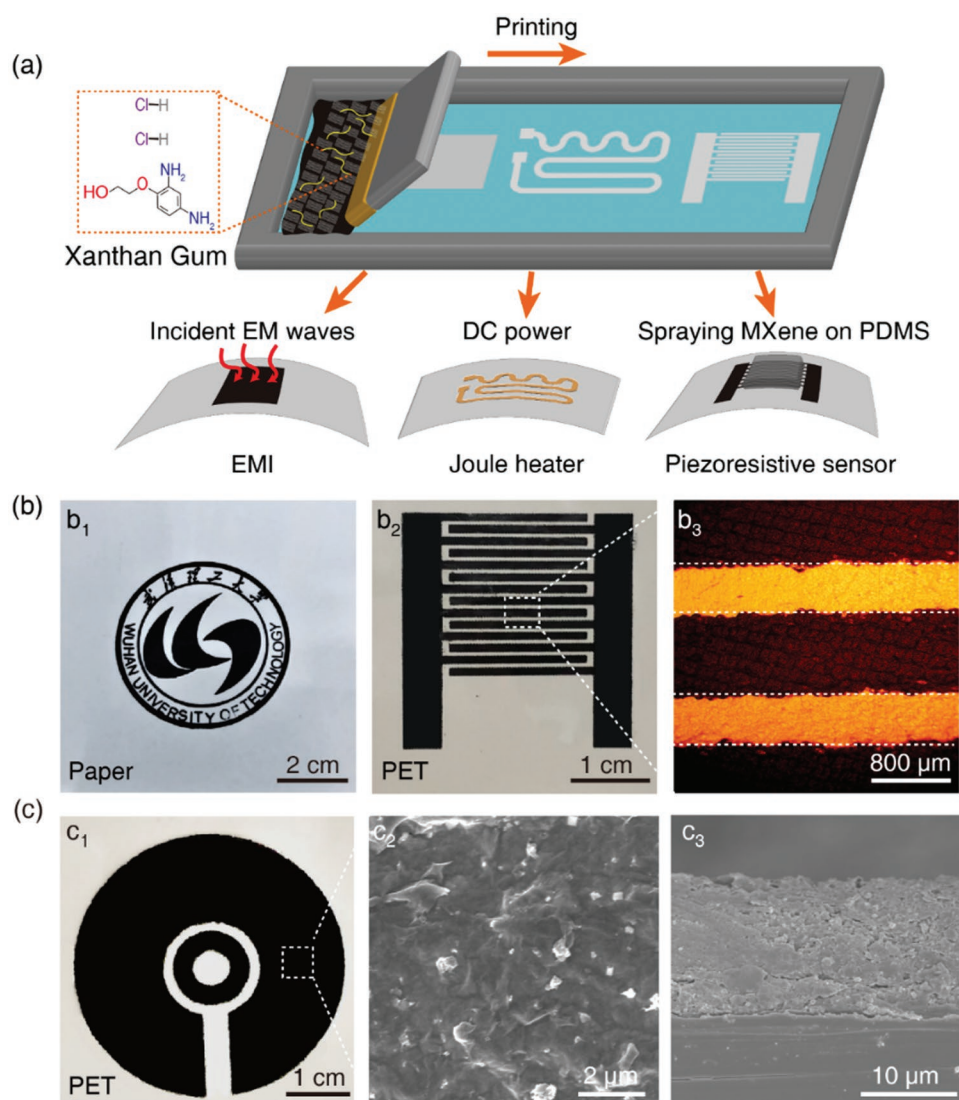


Figure 3. a) Screen-printing flexible MXene patterns for EMI, Joule heater and piezoresistive sensor devices. b,c) Optical photographs of screen-printed MXene patterns with different shapes, b₁) logo of Wuhan University of Technology, b₂) interdigital electrode, b₃) magnified area of the dashed box in (b₃). c₁) Optical, c₂) top-view, and c₃) cross-sectional SEM images of MXene film printed on the PET substrate.

Clearly, cross-sectional SEM examination of printed MXene film (Figure 3c₃ and Figure S7a₄,b₄, Supporting Information) revealed an interconnected scaffold with stacked MXene, without structural collapse. To improve the conductivity of printed MXene film, the residual solvents were further removed by heat treatment after printing. As expected, the sheet resistance of the printed MXene film was initially reduced from 4.72 to 1.74 $\Omega \text{ sq}^{-1}$ after heat treatment for 30 min (Figure S8, Supporting Information), which is associated with the narrowing of interlayer spacing between MXenes induced by the removal of water solvent. When extended to 3h, the sheet resistance was not reduced further but increased to 2.56 $\Omega \text{ sq}^{-1}$, which can be ascribed to the gentle oxidation of MXene after exposure to air.^[29,30] On the other hand, xanthan gum was found to play an important role in improving the processability of screen printing. Hybrid MXene ink exhibited improved adhesion with the substrates as compared to pure MXene inks.^[34,35] Therefore, highly dense and uniform films were achieved for printed

patterns using MXene hybrid inks compared to pure MXene inks. In addition, the edge of printed pattern based on pure MXene ink was slipped, while quite smooth and clear when using MXene-xanthan hybrid inks (Figure S9, Supporting Information). Xanthan gum ensures the accuracy and feasibility of MXene hybrid inks in the printed patterns, which lays a solid foundation for the application of EMI, Joule heater and piezoresistive sensors.

2.3. EMI Shielding Performance of Screen-Printed MXene Film

In general, the intrinsic conductivity and thickness of microwave absorbing materials are the two dominant factors that will influence their EMI shielding performance. As shown in Figure 4a, the average EMI SE values of the MXene films printed on the paper, PET and PI substrates are 40.1, 37.7 and 35.2 dB, respectively. Such superior EMI shielding performance

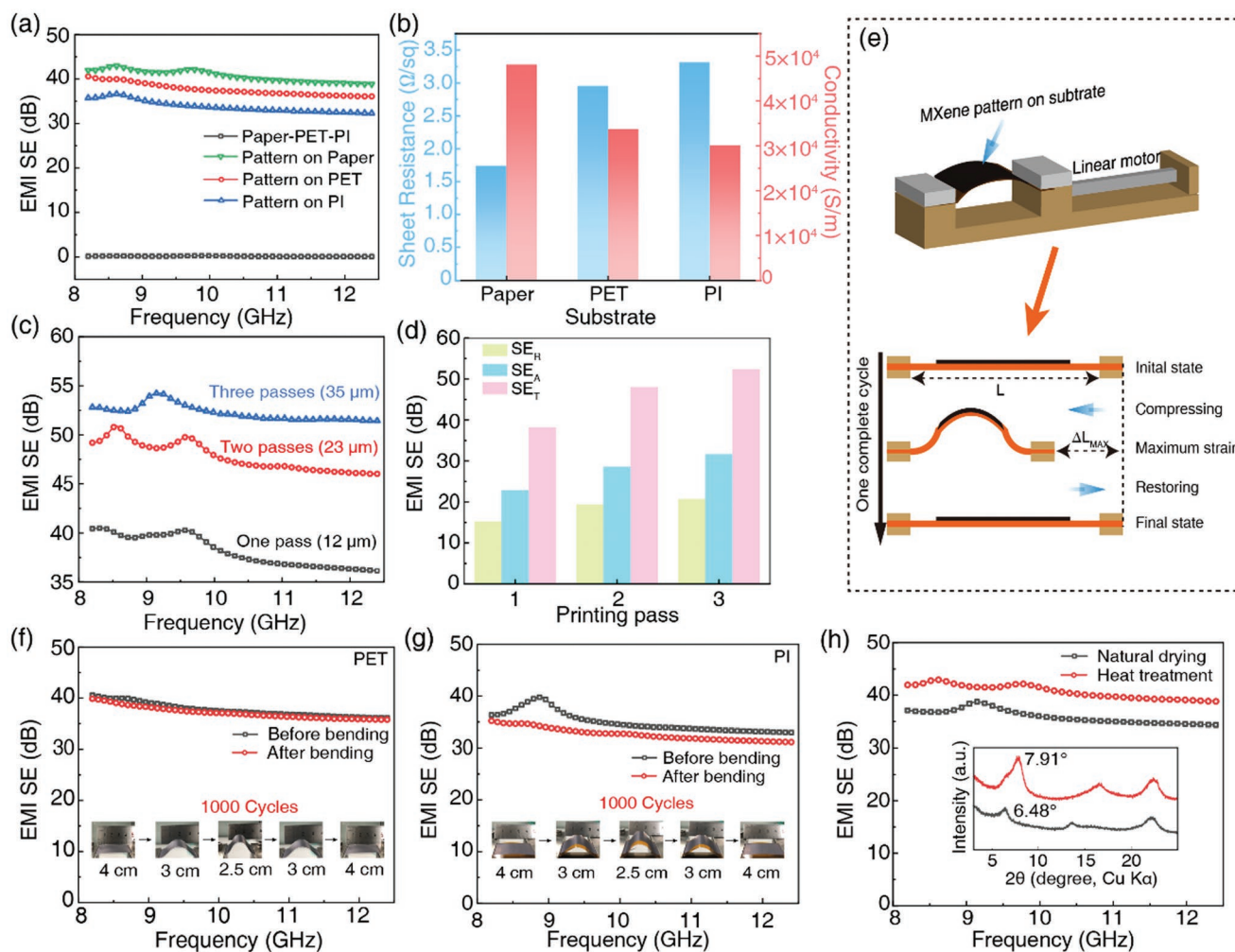


Figure 4. EMI shielding performance of screen-printed MXene films. a) EMI SE of MXene film plotted as a function of frequency between 8.2 and 12.4 GHz. b) Square resistance and conductivity of MXene film printed on paper, PI, and PET substrates. c) Frequency dependence of EMI SE for MXene film printed on paper with different printing passes. d) The average EMI SE_T , SE_A , and SE_R values plotted as a function of printing passes. e) Scheme of bending test for MXene film. Frequency dependency of EMI SE for MXene film printed on f) PET and g) PI substrates before and after bending 1000 cycles. h) Comparison of EMI SE of MXene films by vacuum drying at 120 °C for 30 min with that of natural drying in the frequency range of 8.2–12.4 GHz. Inset: XRD patterns of MXene films before and after heat treatment.

can be attributed to the high electrical conductivity of MXene.^[36] As summarized in Figure 4b, the conductivity of the MXene film printed on paper was $4.8 \times 10^4 \text{ S m}^{-1}$, while those on PET and PI substrates were 3.38×10^4 and $3.1 \times 10^4 \text{ S m}^{-1}$, respectively. Therefore, the EMI shielding performance on different substrates was clearly related to their conductivity. As depicted in Figure 4c, the total EMI SE value increased with the increase of printing passes and approached to 54.2 dB in the case of three printing passes. When an electromagnetic wave is incident on a shielding material, the incident wave is divided into reflected wave, absorbed wave and transmitted power. The overall shielding efficiency (SE_T) includes contributions from absorption (SE_A), reflection (SE_R), and multiple reflection (SE_M). SE_M is often neglected when SE_T is greater than 15 dB.^[37] The average SE_T , SE_A , and SE_R values were summarized in Figure 4d. Because SE_A was related to the thickness of the printed MXene film, the SE_A values of all printed MXene films were found to continually increased with the increase of printing pass, while the SE_R value exhibited slight enhancement tendency. The stacking density of printed MXene film nearly remained unchanged even after multiple printing pass. On the other hand, the SE_R value of all printed MXene films was above 10 dB. This result indicates that more than 90% of the electromagnetic wave will be reflected before entering the films.^[38]

Importantly, the printed MXene films should have satisfactory mechanical flexibility and structural stability to withstand complex deformation such as bending in practical applications. As demonstrated in Figure 4e, cyclic bending tests of these printed MXene films were performed. Figure 4f,g and Figure S10 (Supporting Information) depict the frequency dependence of EMI value for the MXene films before and after bending 1000 cycles. The EMI efficiency of all the printed MXene films can remain above 93.0% after bending 1000 cycles, while a maximum value was up to 98.6% for MXene film printed on PET substrate. MXene films based on hybrid inks exhibited higher average EMI SE values and better bending resistance than pure MXene films (Figure S11, Supporting Information). SEM characterization showed that hybrid film surface was obviously denser (Figure S4, Supporting Information), contributing to higher electrical conductivity. Specially, the EMI efficiency of hybrid films printed on PEI can remain 98.6% after bending 1000 cycles, while only 89.8% for pure MXene films. Such excellent bending durability can be attributed to the strong adhesion between MXene film and flexible substrate. Specially, cross-sectional SEM images of printed MXene film were carried out before and after bending test (Figure S12, Supporting Information). Printed MXene film was still closely attached to the PET substrate without obvious MXene detaching (Figure S12b, Supporting Information). This observation may imply that the adhesion between MXene film and PET substrate is the strongest among them (Figure S12a,S12c, Supporting Information). As depicted in Figure 4h, the EMI SE value of printed MXene film was increased from 35.9 to 40.7 dB after heat treatment. XRD patterns of printed MXene film in the inset of Figure 4h revealed the possible origin for such change in the EMI performance. After heat treatment at 120 °C, the 002 peak in the printed MXene film shifted from 6.48° to 7.91°, which was associated with a decreased interlayer

spacing from 1.36 to 1.11 nm. In this context, denser stacking of MXene in printed film was induced by heat treatment, leading to the decrease of contact resistance and the increase of EMI shielding performance.

2.4. Joule Heating Performance of Screen-Printed MXene Film

Printed MXene films with high conductivity also display excellent Joule heating performance ($Q = U^2t/R$, where Q is the generated Joule heat, U is the DC voltage, R is the resistance, t is the working time), which is suitable for automatic heating clothing and thermotherapy.^[39] Figure 5 shows the Joule heating performance of printed MXene films, and the measured MXene-based patterns were the concentric rings shown in Figure 3c₁, Figure 5a and Figure S13 (Supporting Information) show the infrared (IR) thermal images of the printed MXene films driven by different applied voltages. Obviously, the thermal images revealed uniform temperature distribution when the current passes, which also proved the uniform distribution of MXene in the printed film. As for MXene films printed on paper, PET, and PI substrates, the temperature was increased from room temperature to 130.8, 98.2, and 84.3 °C when the applied voltage was increased from 1 to 4 V (Figure 5b), respectively. Meanwhile, the maximum temperature for pure MXene film printed on paper and PET was only 115.1 and 84 °C (Figure S14, Supporting Information). Generally, thermal conductivity is strongly related to the electrical conductivity in MXene. So, the thermal conductivity of printed MXene films is very high, while PET and PI substrates rather low. This MXene/polymer interface can reduce the thermal conductivity caused by phonon scattering and phonon mismatch in MXene/polymer film devices.^[40] In this case, the heat can be quickly transferred inside the printed film without diffusing to the substrate, realizing the high heating rate driven by low voltage in the printed MXene film. A rapid thermal response time within 10 s was achieved in all the printed MXene films, regardless of the applied voltage. According to Joule's law, a higher applied DC voltage will lead to a higher steady-state temperature (SSTs). A maximum heating rate of MXene film printed on paper can reach up to 20 °C s⁻¹ when driven by a DC voltage of 4 V. Moreover, Figure 5c shows a linear relationship between the steady-state temperature and the square of the voltage, which is consistent with Joule's law. Figure 5d shows the variation of current with respect to the driven voltages, with a linear relationship indicating good stability of the resistance of printed MXene film. A long-term stability of printed MXene film was realized under an applied voltage of 2.5 V (Figure 5e), without large temperature fluctuations during the test more than 6 h. This Joule thermal performance was compared with those reported in other literatures in the Table S1 (Supporting Information), in which the steady-state temperature and the maximum heating rate were used to evaluate the electrothermal efficiency. The higher electrical conductivity of MXene enables excellent performance as Joule heater, superior to other materials such as CNT, graphene film, rGO film and conducting polymer.^[41]

On the other hand, the de-icing experiment was performed on the printed MXene films to demonstrate the potential for

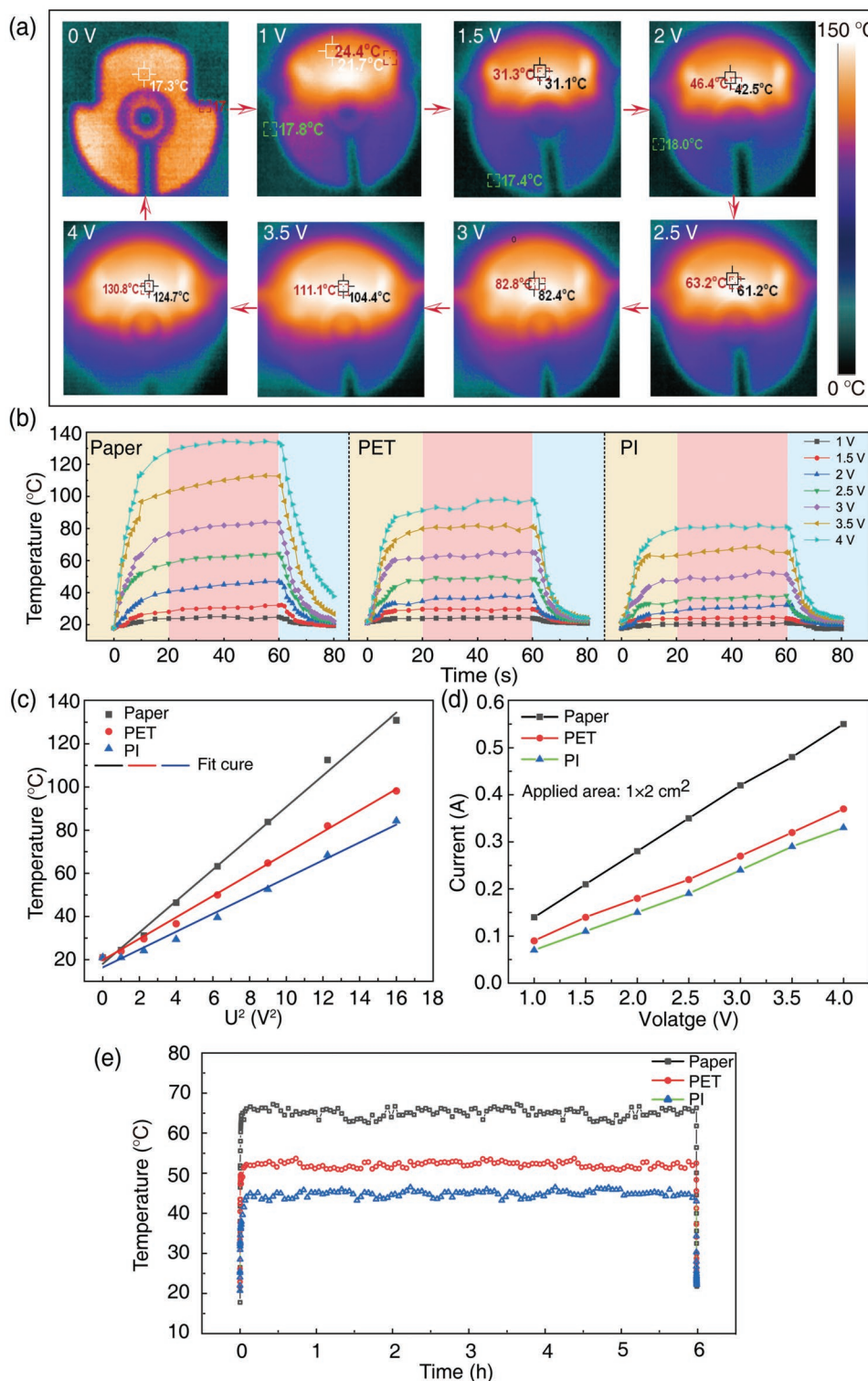


Figure 5. Joule heating performance of MXene film printed on different substrates. a) IR thermal images of MXene film on paper recorded at a stepwise enhancement of voltage from 1 to 4 V. b) Temperature-time curves of MXene film under different working voltages. c) The linear fitting of saturation temperature versus U^2 and d) I - V curves of MXene film. e) Long-term stability of temperature for MXene film driven by an applied voltage of 2.5 V.

application as Joule heater. The ice block was placed on the printed MXene film driven by a DC voltage of 2.5 V, which quickly melt in a significantly faster rate than that of the

unheated ice block (Figure S15, Supporting Information). After heating for about 19 min, the ice block completely melted into liquid, while the unheated ice block transformed into liquid

only after about 53 min. Meanwhile, the temperature of liquid water after heating ablation has increased up to 33.1 °C (Figure S15, Supporting Information). The melting rate was about three times faster than the natural melting rate. This observation confirms that the printed MXene film has good heating performance at low voltage of 2.5 V. Therefore, Joule heating response with excellent cycle stability at low voltage can meet the reliability requirement of various scenarios.

2.5. Pressure-Sensing Performance of Screen-Printed MXene Film

For the wearable piezoresistive sensors, the flexible electrode is critical for commercialization.^[42] Combined with the roughness of air-laid paper, we designed high-performance piezoresistive sensor based on screen-printed MXene film. The interdigitated electrode based on MXene and the performance of piezoresistive

sensor were investigated, as shown in Figure 6a. To understand the interaction mechanism of piezoresistive sensor, the surface morphology of the sensing layer (air-laid paper-PDMS) were analyzed by three-dimensional ultra-depth-of-field optical microscope and SEM, as shown in Figure 6b,c, respectively. The surface of air-laid paper-PDMS was randomly distributed with microscopic protrusions, which is suitable to construct piezoresistive sensor with high sensitivity. In addition, the corresponding mapping of C, Ti, O, and F elements suggests that MXene was uniformly sprayed on the air-laid paper-PDMS (Figure 6d). The piezoresistive pressure sensor converts the applied pressure stimulus into the change of an electrical signal.^[43] At the initial state, there were only a few contact points between air-laid paper-PDMS and printed interdigitated electrode with the absence of the external applied force. With the increase of applied force, the conductive area of the interface continued to increase, leading to the decrease in the resistance as shown in Figure S16 (Supporting Information).

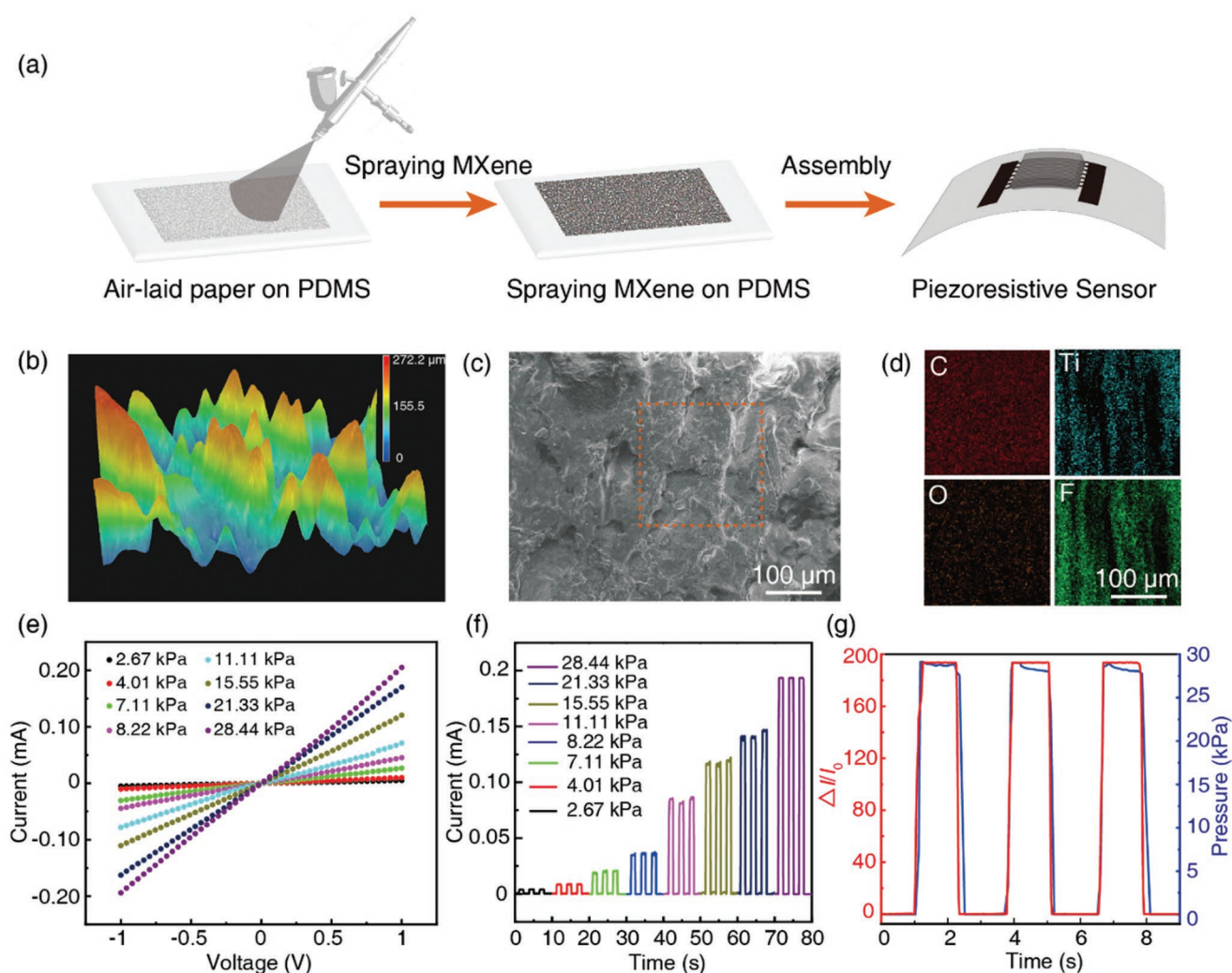


Figure 6. Sensing performance of MXene piezoresistive sensor. a) Fabrication diagram of MXene piezoresistive sensor. b) 3D structure diagram of air-laid paper embedded on PDMS c) SEM images of MXene sprayed on PDMS. d) Mapping of C, Ti, O, and F elements corresponding to the dashed frame in (c). e) I - V and f) I - T curves of air-laid paper sensor under different pressures. g) Variation of current and pressure under periodic loading and unloading conditions. The measured frequency is 0.44 Hz.

The overall equivalent circuit resistance of piezoresistive sensors can be described below:

$$R = R_i + \frac{R_s R_b}{R_s + R_b} \quad (1)$$

where R_i is the intrinsic resistance of the printed electrode, R_s and R_b are the resistance of the conductive paths, which increase with loading and unloading state, respectively. During the loading of the applied force onto the sensor, R_i remained unchanged. A smaller R_i will induce a higher sensitivity of the piezoresistive sensor.^[44,45] On the other hand, a continuous increase of the contact area between the prominent structure and the electrode will result in the increase of the conductivity of the channels.

Figure 6e shows the I - V curves of MXene-based sensors under different pressures. The linear relationship observed indicates a good Ohmic contact between MXene sensor and the printed interdigitated electrodes. Figure 6f shows the I - T curves of MXene-based sensor under continuous enhancement of the applied pressures below 30 kPa. The current increased with the increase of the applied pressure, implying an increasing contact area between air-laid paper-PDMS and interdigitated electrode. In terms of the change in current, the strength of the external pressure applied on the sensor can be directly monitored. In addition, another important parameter for evaluating the sensor is the response time. Ideally, fast response without delay ensures the timely response under the external pressure. In real measurement, the elastic deformation of air-laid paper-PDMS substrate will lead to a certain delay of response time. The response and recovery time of the MXene sensor were only 125 and 104 ms under 7.11 kPa (Figure S17, Supporting Information), respectively. Such fast response is sufficient to meet the requirement for practical application. Under the periodic pressure test with a certain frequency, the coincided I - T and P - T curves in Figure 6g further proves the rapid response time and good sensing performance of MXene-based piezoresistive sensor. In actual applications, the change of current during the finger tapping, wrist and finger bending was detected quickly, and the corresponding real-time signals remained almost the same for the cyclic bending activities, indicating the outstanding stability of our sensor (Figure S18, Supporting Information). Therefore, the piezoresistive sensor can easily detect human activities. In addition, the piezoresistive sensor can work stably under different pressures and exhibit excellent cycle stability (Figure S19, Supporting Information).

3. Conclusion

In summary, we demonstrated the design of aqueous MXene hybrid inks for screen printing of flexible patterns, which exhibited excellent flexibility and high conductivity up to $4.8 \times 10^4 \text{ S m}^{-1}$. By assembling the printed film into multifunctional devices, they displayed excellent EMI shielding efficiency, Joule heating ability, and sensing performance. The EMI shielding performance of printed MXene film can reach to 54.2 dB, without significant performance decay after bending 1000 cycles. In terms of Joule heater application, the heating rate of printed device can reach $20 \text{ }^\circ\text{C s}^{-1}$ under a driving

voltage of 4 V, with the highest steady-state temperature of $130.8 \text{ }^\circ\text{C}$. The Joule heater can generate a pleasant heating temperature under low operating voltage below 2.5 V. As for the printed MXene pressure sensor, its response time was less than 130 ms, while the pressure response was below 30 kPa. Therefore, the flexible devices exhibited excellent electrical and electromagnetic shielding properties, low-voltage-driven heating performance and sensing performance. Screen-printed MXene patterns were promising for the next generation of flexible and wearable electronics.

4. Experimental Section

Synthesis of $\text{Ti}_3\text{C}_2\text{T}_x$: The etching of MAX phase was carried out using a minimally intensive layer delamination or mild synthesis route.^[21] Typically, LiF (99.99%, Sigma Aldrich) was slowly added to 9 M HCl (37 wt%, Sinopharm Chemical) under vigorous stirring at 500 rpm for 30 min. Ti_3AlC_2 MAX phase (11 Technology) was then slowly added to the above mixture under vigorous stirring at 500 rpm, and reacted at $35 \text{ }^\circ\text{C}$ for 48 h. After etching, the supernatant was centrifuged at 3500 rpm for 5 min with ultrapure water. The above procedures were repeated until the pH of the supernatant was 6–7. After ultrasonic stratification at 576 W for 30 min, the suspension was then centrifuged at 3500 rpm for another 30 min. The resultant colloidal solution was freeze-dried to obtain $\text{Ti}_3\text{C}_2\text{T}_x$ powder.

Ink Formulation of $\text{Ti}_3\text{C}_2\text{T}_x$: The xanthan gum aqueous solution with a concentration of 2 mg mL^{-1} was prepared by stirring for 30 min at a speed of 2000 r min^{-1} and then defoamed for several minutes using a planetary agitator. Freeze-dried MXene powder was subsequently added to xanthan gum aqueous solution, and mixed by planetary agitator at a rate of 2000 r min^{-1} for 30 min. MXene inks with controlled concentration and weight ratio of MXene to xanthan gum were obtained.

Screen Printing of MXene Patterns: The printing template was made of 200-mesh stainless steel frame, which meets certain printing accuracy. The printed patterns were composed of simple line with widths ranging from 200 to 1000 μm . The rectangular patterns of $20 \times 30 \text{ mm}^2$ were designed to fabricate various devices, such as electromagnetic shielding, interdigital electrodes with a line width of 1 mm and piezoresistive sensors with a spacing of 0.5 mm. The PET and PI substrates were treated by UV to enhance the adhesion between MXene and them. Upon dropping MXene ink slurry on the side of screen, a squeegee was then applied to print various MXene patterns under a velocity of 2 cm s^{-1} . After each printing, the MXene patterns were solidified by blowing 10 min, followed by heat treatment in vacuum oven at $120 \text{ }^\circ\text{C}$ for 30 min to completely remove water solvent.

Preparation of MXene Piezoresistive Sensor: To increase the roughness of polydimethylsiloxane (PDMS), air-laid paper was embedded into the curing PDMS. The MXene suspension (5 mg mL^{-1}) was sprayed onto the air-laid paper-PDMS, which was assembled with the printed interdigital electrodes to form a piezoresistive sensor.

Characterizations: The morphology and crystal structure of MXene and printed films were carried out using SEM (Zeiss Ultra Plus), and TEM (Talos F200S). The morphology and thickness of MXene were measured by AFM (Cypher ES) in a standard tapping mode. The crystal structure of powder samples was evaluated by XRD (Rigaku Smartlab). The chemical elements and surface covalent bonding of $\text{Ti}_3\text{C}_2\text{T}_x$ powder were detected by XPS (ESCALAB 250Xi). The viscosity and elastic modulus of MXene inks were performed by Dynamic Shear Rheometer (Anton Paar, SmartPave 92). The resistance of printed MXene films was measured by a four-point probe instrument (RTS-9) with a probe distance of 1 mm. The thickness of printed MXene films was collected by the micrometer with 0.1 μm accuracy.

Electromagnetic parameters of screen-printed MXene films were obtained using a network analyzer (PNA Network Analyzer, N5244B) in the frequency range of 8.2–12.4 GHz (X-band) at room temperature.

The vector network analyzer outputs in the form of four scattering parameters (S_{11} , S_{12} , S_{21} , S_{22}). SE_R and SE_A represent the effectiveness of reflection and absorption, respectively. The power of incident electromagnetic wave in the shielding material was expressed as:

$$R = |S_{11}|^2, T = |S_{21}|^2 \quad (2)$$

$$A = 1 - R - T \quad (3)$$

$$SE_T = SE_R + SE_A + SE_M \quad (4)$$

$$SE_R = -10 \log(1 - R) \quad (5)$$

$$SE_A = -10 \log \frac{T}{1 - R} \quad (6)$$

SE_T is the sum of SE_R , SE_A , and SE_M contributions. SE_M is assumed to be zero when SE_T is greater than 15 dB.^[46]

Joule heating performance was characterized by charging under a certain voltage supplied by DC power (Rigol, DP832), and monitored by the variation of surface temperature captured by thermal imaging camera (Fluke). The sensing performance of piezoresistive sensor was recorded by a test system consisting of a computer-controlled stepping motor, a dynamometer and a constant current source (Agilent B2901A).

Supporting Information

Supporting Information is available from the Wiley Online Library or from the author.

Acknowledgements

This work was supported by the National Key Research and Development Program of China (2020YFA0715000), Basic Science Center Program of NSFC (Grant No. 51788104), the National Natural Science Foundation of China (Grant Nos. 52172124, 51872214, and 51802237), and the Fundamental Research Funds for the Central Universities (WUT: 2021111019JC, 2018111041GX).

Conflict of Interest

The authors declare no conflict of interest.

Data Availability Statement

The data that support the findings of this study are available from the corresponding author upon reasonable request.

Keywords

electromagnetic interference shielding, Joule heater, MXene ink, piezoresistive sensor, screen printing

Received: November 16, 2021

Revised: January 21, 2022

Published online:

[1] C. Wu, T. Kim, F. Li, T. Guo, *ACS Nano* **2016**, *10*, 6449.

[2] D. Zhao, Y. Zhu, W. Cheng, W. Chen, Y. Wu, H. Yu, *Adv. Mater.* **2021**, *33*, 2000619.

- [3] S. Uzun, M. Schelling, K. Hantanasirisakul, T. S. Mathis, R. Askeland, G. Dion, Y. Gogotsi, *Small* **2021**, *17*, 2006376.
- [4] W. Wang, P. Pfeiffer, L. Schmidt-Mende, *Adv. Funct. Mater.* **2020**, *30*, 2002685.
- [5] M. Vural, A. Pena-Francesch, J. Bars-Pomes, H. Jung, H. Gudapati, C. B. Hatter, B. D. Allen, B. Anasori, I. T. Ozbolat, Y. Gogotsi, M. C. Demirel, *Adv. Funct. Mater.* **2018**, *28*, 1801972.
- [6] M. Hossain, K. P. Sibin, K. D. M. Rao, *J. Mater. Chem. C* **2021**, *9*, 6257.
- [7] Y. Xu, Y. Ang, L. Wu, L. K. Ang, *Nanomaterials* **2019**, *9*, 165.
- [8] H. Zhao, R. Hu, P. Li, A. Gao, X. Sun, X. Zhang, X. Qi, Q. Fan, Y. Liu, X. Liu, M. Tian, G. Tao, L. Qu, *Nano Energy* **2020**, *76*, 104926.
- [9] Y. Ma, J. Ouyang, T. Raza, P. Li, A. Jian, Z. Li, H. Liu, M. Chen, X. Zhang, L. Qu, M. Tian, G. Tao, *Nano Energy* **2021**, *85*, 105941.
- [10] X. Qing, Z. N. Chen, C. K. Goh, *Electron. Lett.* **2010**, *46*, 1591.
- [11] S. Koochi-Fayegh, M. A. Rosen, *J. Energy Storage* **2020**, *27*, 101047.
- [12] G. Hu, J. Kang, L. W. T. Ng, X. Zhu, R. C. T. Howe, C. G. Jones, M. C. Hersam, T. Hasan, *Chem. Soc. Rev.* **2018**, *47*, 3265.
- [13] Q. Yang, Y. Wang, X. Li, H. Li, Z. Wang, Z. Tang, L. Ma, F. Mo, C. Zhi, *Energy Environ. Sci.* **2018**, *11*, 183.
- [14] Y. Zhang, Y. Wang, Q. Jiang, J. K. El-Demellawi, H. Kim, H. N. Alshareef, *Adv. Mater.* **2020**, *32*, 1908486.
- [15] S. Abdolhosseinzadeh, X. Jiang, H. Zhang, J. Qiu, C. Zhang, *Mater. Today* **2021**, *48*, 214.
- [16] Q. Huang, Y. Zhu, *Adv. Mater. Technol.* **2019**, *4*, 1800546.
- [17] H. Li, X. Li, J. Liang, Y. Chen, *Adv. Energy Mater.* **2019**, *9*, 1803987.
- [18] M. Naguib, M. Kurtoglu, V. Presser, J. Lu, J. Niu, M. Heon, L. Hultman, Y. Gogotsi, M. W. Barsoum, *Adv. Mater.* **2011**, *23*, 4248.
- [19] M. Naguib, V. N. Mochalin, M. W. Barsoum, Y. Gogotsi, *Adv. Mater.* **2014**, *26*, 992.
- [20] S. Shen, T. Ke, K. Rajavel, K. Yang, D. Lin, *Small* **2020**, *16*, 2002433.
- [21] K. Hantanasirisakul, Y. Gogotsi, *Adv. Mater.* **2018**, *30*, 1804779.
- [22] M. Ghidui, M. R. Lukatskaya, M. Zhao, Y. Gogotsi, M. W. Barsoum, *Nature* **2014**, *516*, 78.
- [23] X. Wu, T. Tu, Y. Dai, P. Tang, Y. Zhang, Z. Deng, L. Li, H. Zhang, Z. Yu, *Nano-Micro Lett.* **2021**, *13*, 148.
- [24] V. T. Nguyen, Q. Nguyen, B. Min, Y. Yi, C. Choi, *Chem. Eng. J.* **2022**, *430*, 133171.
- [25] Y. Chen, Y. Li, Y. Liu, P. Chen, C. Zhang, H. Qi, *ACS Appl. Mater. Interfaces* **2021**, *13*, 36221.
- [26] S. Abdolhosseinzadeh, R. Schneider, A. Verma, J. Heier, F. Nüesch, C. Zhang, *Adv. Mater.* **2020**, *32*, 2000716.
- [27] T. Qiu, G. Li, Y. Shao, K. Jiang, F. Zhao, F. Geng, *Carbon Energy* **2020**, *2*, 624.
- [28] V. Kamysbayev, A. S. Filatov, H. Hu, X. Rui, F. Lagunas, D. Wang, R. F. Klie, D. V. Talapin, *Science* **2020**, *369*, 979.
- [29] Y. Chae, S. Kim, S. Cho, J. Choi, K. Maleski, B. Lee, H. Jung, Y. Gogotsi, Y. Lee, C. Ahn, *Nanoscale* **2019**, *11*, 8387.
- [30] I. Persson, L. Näslund, J. Halim, M. W. Barsoum, V. Darakchieva, J. Palisaitis, J. Rosen, P. Persson, *2D Mater.* **2015**, *5*, 015002.
- [31] W. Chen, S. Lai, C. Yen, X. Jiang, D. Peroulis, L. Stanciu, *ACS Nano* **2020**, *14*, 11490.
- [32] W. Wang, *Prog. Mater. Sci.* **2012**, *57*, 487.
- [33] E. Quain, T. Mathis, N. Kurra, K. Maleski, K. L. Aken, M. Alhabeib, H. N. Alshareef, Y. Gogotsi, *Adv. Mater. Technol.* **2019**, *4*, 1800256.
- [34] J. Zhang, N. Kong, S. Uzun, A. Levitt, S. Seyedin, P. A. Lynch, S. Qin, M. Han, W. Yang, J. Liu, X. Wang, Y. Gogotsi, J. M. Razal, *Adv. Mater.* **2020**, *32*, 2001093.
- [35] S. A. Mirkhani, A. S. Zeraati, E. Aliabadian, M. Naguib, U. Sundararaj, *ACS Appl. Mater. Interfaces* **2019**, *11*, 18599.
- [36] G. Weng, J. Li, M. Alhabeib, C. Karpovich, H. Wang, J. Lipton, K. Maleski, J. Kong, E. Shauly, M. Elimelech, Y. Gogotsi, A. D. Taylor, *Adv. Funct. Mater.* **2018**, *28*, 1803360.

- [37] Z. Chen, C. Xu, C. Ma, W. Ren, H. Cheng, *Adv. Mater.* **2013**, *25*, 1296.
- [38] D. D. L. Chung, *Carbon* **2001**, *39*, 279.
- [39] X. Zhao, L. Wang, C. Tang, X. Zha, Y. Liu, B. Su, K. Ke, R. Bao, M. Yang, W. Yang, *ACS Nano* **2020**, *14*, 8793.
- [40] L. Yan, M. Shao, H. Wang, D. Dudis, A. Urbas, B. Hu, *Adv. Mater.* **2011**, *23*, 4120.
- [41] B. Shi, Y. Shang, P. Zhang, A. Cuadros, J. Qu, B. Sun, B. Gu, T. Chou, K. Fu, *Matter* **2020**, *2*, 1594.
- [42] Y. Ma, N. Liu, L. Li, X. Hu, Z. Zou, J. Wang, S. Luo, Y. Gao, *Nat. Commun.* **2017**, *8*, 1207.
- [43] H. Zhao, X. Qi, Y. Ma, X. Sun, X. Liu, X. Zhang, M. Tian, L. Qu, *Nano Lett.* **2021**, *21*, 8126.
- [44] Z. Lou, S. Chena, L. Wang, K. Jiang, G. Shen, *Nano Energy* **2016**, *23*, 7.
- [45] Y. Cheng, Y. Ma, L. Li, M. Zhu, Y. Yue, W. Liu, L. Wang, S. Jia, C. Li, T. Qi, J. Wang, Y. Gao, *ACS Nano* **2020**, *14*, 2145.
- [46] M. Cao, Y. Cai, P. He, J. Shu, W. Cao, J. Yuan, *Chem. Eng. J.* **2019**, *359*, 1265.